

Deconvolution reconstruction of full-view and limited-view photoacoustic tomography: a simulation study

Chi Zhang and Yuanyuan Wang*

Department of Electronic Engineering, Fudan University, Shanghai, 200433, China

*Corresponding author: yzwang@fudan.edu.cn

Received March 4, 2008; revised July 6, 2008; accepted July 15, 2008;
posted July 18, 2008 (Doc. ID 93433); published September 11, 2008

Although many algorithms are available for full-view photoacoustic tomography (PAT), no exact and stable algorithm for limited-view PAT has been proposed. In this paper the deconvolution reconstruction (DR) algorithm is proposed for both full-view and limited-view PAT. In the DR algorithm, first a new function is constructed from detected photoacoustic signals and approximately simplified, and then the tissue's electromagnetic absorption is derived from this function on the basis of Fourier-based deconvolution. Computer simulations are carried out to compare the DR algorithm with two popular PAT algorithms, the time-domain reconstruction (TDR) and the filtered back projection (FBP). Although the error of the DR algorithm increases with the size of the detected object, it is shown that the DR algorithm has good precision and strong robustness to noise in the full-view PAT, nearly equivalent to the TDR and FBP. Yet the DR algorithm is more than ten times faster in computation speed. In the limited-view PAT, the DR is superior to the TDR and FBP in terms of both accuracy and robustness to noise. © 2008 Optical Society of America

OCIS codes: 170.3010, 170.3880, 170.5120, 170.6960.

1. INTRODUCTION

Photoacoustic imaging (PAI), which is also often referred to as thermoacoustic imaging, is a new fast-developing technique of noninvasive medical imaging [1–6]. In the typical PAI of biological tissues, a short-pulsed electromagnetic wave (usually laser or microwave) is employed to irradiate the tissue. Absorbing the electromagnetic energy, the tissue radiates photoacoustic waves (normally ultrasound waves), which carry the electromagnetic absorption property of the tissue, by thermoelastic expansion. Then an ultrasonic transducer (or sometimes a transducer array for fast imaging [3]) is employed to acquire photoacoustic signals, from which the electromagnetic absorption distribution image of the tissue can be reconstructed. Combining the high contrast of optical imaging and the high resolution of ultrasound imaging, PAI is very efficient in the applications of breast tumor detection [7] and blood vessel imaging [8,9]. It has also been applied to *in vivo* imaging of rat brain [10] and *in vitro* flow measurements [5].

Photoacoustic tomography (PAT) and photoacoustic microscopy (PAM) are two main techniques of PAI. The former normally uses an unfocused ultrasonic transducer to scan around the tissue and provides a high-resolution image of the whole tissue in the detection region, while the latter uses a focused ultrasonic transducer and focuses on imaging the microvascular structure of body surface [9]. This paper studies mainly the PAT reconstruction algorithm, which aims at reconstructing the electromagnetic absorption distribution from detected photoacoustic waves, a key problem of PAT.

By now, there already exist many exact and approxi-

mate algorithms for PAT when the ultrasonic transducer collects signals along a sphere, plane, or cylinder in the three-dimensional (3-D) case or along a circle or line in the two-dimensional (2-D) case [11–19]. In all exact algorithms, it is assumed that photoacoustic signals are detected from a full view, 4π sr in the 3-D case or 2π rad in the 2-D case. However, photoacoustic signals cannot be detected from a full view in many applications, such as the detection of human breast. In the limited-view PAT, applying algorithms of the full-view PAT will cause boundaries and sharp details to become blurred [20]. So far, to the best of our knowledge, no exact and stable algorithm for the limited-view PAT has been proposed.

In this paper, a novel reconstruction algorithm, the deconvolution reconstruction (DR), is proposed for PAT when the ultrasonic transducer scans along a sphere in the 3-D case or a circle in the 2-D case. The key step of the DR algorithm is the Fourier-based deconvolution. As a fast approximate algorithm, the DR is proved to have good precision and low noise sensitivity for both the full-view and limited-view cases. Simulation studies are conducted, and the results confirm our theoretical prediction.

2. THEORY

A. DR Algorithm for the Full-View PAT

The DR algorithm is derived in the 3-D case. Assuming that the biological tissue is irradiated by the short-pulsed electromagnetic wave homogeneously and the sound speed in the tissue is invariable, the relation between the excited acoustic pressure $p(\mathbf{r}, t)$ at position \mathbf{r} and the spatial distribution of the electromagnetic absorption $A(\mathbf{r})$ is given by [11,12]

$$p(\mathbf{r}, t) = \frac{\beta}{4\pi C_p} \int \int \int \frac{d^3 \mathbf{r}'}{|\mathbf{r} - \mathbf{r}'|} A(\mathbf{r}') I' \left(t - \frac{|\mathbf{r} - \mathbf{r}'|}{c} \right), \quad (1)$$

where t is the time, $I(t)$ is the electromagnetic pulse function, β is the coefficient of volumetric thermal expansion, c is the sound speed, C_p is the specific heat, r' is the integral variable, and $I'(\cdot)$ is the derivative of $I(\cdot)$. The PAT algorithm is a typical inverse problem of deriving $A(\mathbf{r})$ from $p(\mathbf{r}, t)$.

It is usually assumed that the electromagnetic pulse function is a Dirac delta function and the radiation begins at $t=0$, i.e., $I(t) = \delta(t)$. Moreover, the ultrasonic transducer moves along a spherical surface whose radius is r_0 and center of the sphere is the origin. So it satisfies that $\mathbf{r} = \mathbf{r}_0$ in $p(\mathbf{r}, t)$. Then Eq. (1) can be simplified to [12,16]

$$p(\mathbf{r}_0, t) = \frac{\beta}{4\pi C_p c} \frac{\partial}{\partial t} \oint_{|\mathbf{r}' - \mathbf{r}_0| = ct} \frac{A(\mathbf{r}')}{t} d^2 \mathbf{r}'. \quad (2)$$

Equation (2) can be rewritten as

$$\left[\int_0^t p(\mathbf{r}_0, t) dt \right] \cdot t = \eta \oint_{|\mathbf{r}' - \mathbf{r}_0| = ct} A(\mathbf{r}') d^2 \mathbf{r}', \quad (3)$$

where $\eta = \beta/(4\pi C_p c)$.

Defining

$$S(\mathbf{r}_0, t) = \left[\int_0^t p(\mathbf{r}_0, t) dt \right] \cdot t = \eta \oint_{|\mathbf{r}' - \mathbf{r}_0| = ct} A(\mathbf{r}') d^2 \mathbf{r}'. \quad (4)$$

Then a new function $C(\mathbf{r})$ is constructed as

$$C(\mathbf{r}) = S \left(\frac{\mathbf{r}}{|\mathbf{r}|} \cdot \mathbf{r}_0, \frac{\mu - |\mathbf{r}|}{c} \right), \quad (5)$$

where μ is an arbitrary constant, satisfying that $\mu \geq 2r_0$. Obviously $S(\mathbf{r}_0, t)$ is not equal to zero only if $(r_0 - |\mathbf{r}'|_{\max})/c < t < (r_0 + |\mathbf{r}'|_{\max})/c$, so $C(r)$ has nonzero values only if

$$\mu - |\mathbf{r}'|_{\max} - r_0 < |\mathbf{r}| < \mu + |\mathbf{r}'|_{\max} - r_0. \quad (6)$$

Substituting Eq. (4) into Eq. (5), it is obtained that

$$C(\mathbf{r}) = \eta \oint_{\Omega} A(\mathbf{r}') d^2 \mathbf{r}', \quad (7)$$

where Ω is the integral surface: $|\mathbf{r}' - \mathbf{r}_0|/|\mathbf{r}| = \mu - |\mathbf{r}|$. For the tissue that is included in the scanning sphere, it satisfies that $|\mathbf{r}'|_{\max} < r_0$ ($|\mathbf{r}'|_{\max}$ is the furthest distance between the tissue and the center of scanning circle). Based on Taylor series expansion, it can be obtained that

$$\begin{aligned} \left| \mathbf{r}' - \frac{\mathbf{r}}{|\mathbf{r}|} \cdot \mathbf{r}_0 \right| &= \sqrt{|\mathbf{r}'|^2 + r_0^2 - 2 \frac{\mathbf{r}' \cdot \mathbf{r}}{|\mathbf{r}|} \cdot r_0} \\ &= r_0 \cdot \sqrt{1 - 2 \frac{\mathbf{r}' \cdot \mathbf{r}}{|\mathbf{r}| \cdot r_0} + \frac{|\mathbf{r}'|^2}{r_0^2}} \\ &= r_0 \cdot \left(1 - \frac{\mathbf{r}' \cdot \mathbf{r}}{|\mathbf{r}| \cdot r_0} + \phi(\mathbf{r}', \mathbf{r}, r_0) \right) \\ &= r_0 - \frac{\mathbf{r}' \cdot \mathbf{r}}{|\mathbf{r}|} + r_0 \cdot \phi(\mathbf{r}', \mathbf{r}, r_0), \end{aligned} \quad (8)$$

where $\phi(\mathbf{r}', \mathbf{r}, r_0)$ is a small positive quantity and approaches zero if $|\mathbf{r}'|_{\max} \ll r_0$. If a large μ is chosen in Eq. (5) or the detected tissue is small, thereby satisfying that $2|\mathbf{r}'|_{\max} < \mu - r_0$, it can be obtained that $|\mathbf{r}| > |\mathbf{r}'|_{\max}$ by using Eq. (6). So

$$\begin{aligned} |\mathbf{r} - \mathbf{r}'| &= \sqrt{|\mathbf{r}|^2 + |\mathbf{r}'|^2 - 2\mathbf{r} \cdot \mathbf{r}'} \\ &= |\mathbf{r}| \cdot \sqrt{1 - 2 \frac{\mathbf{r} \cdot \mathbf{r}'}{|\mathbf{r}|^2} + \frac{|\mathbf{r}'|^2}{|\mathbf{r}|^2}} \\ &= |\mathbf{r}| \cdot \left(1 - \frac{\mathbf{r} \cdot \mathbf{r}'}{|\mathbf{r}|^2} + \varphi(\mathbf{r}, \mathbf{r}') \right) \\ &= |\mathbf{r}| - \frac{\mathbf{r} \cdot \mathbf{r}'}{|\mathbf{r}|} + |\mathbf{r}| \cdot \varphi(\mathbf{r}, \mathbf{r}'), \end{aligned} \quad (9)$$

where $\varphi(\mathbf{r}, \mathbf{r}')$ is a small positive quantity and approaches zero if $|\mathbf{r}'|_{\max} \ll |\mathbf{r}|$. Based on Eqs. (8) and (9), the integral surface Ω can be rewritten as

$$|\mathbf{r} - \mathbf{r}'| + [r_0 \cdot \phi(\mathbf{r}', \mathbf{r}, r_0) - |\mathbf{r}| \cdot \varphi(\mathbf{r}, \mathbf{r}')] = \mu - r_0. \quad (10)$$

The second term on the left side of Eq. (10), which is the difference of two small positive quantities, can be approximated to zero. (However, the error will be enlarged when the tissue is large or μ is set to a small value approaching $2r_0$). Then Eq. (7) can be rewritten as

$$C(\mathbf{r}) = \eta \oint_{|\mathbf{r} - \mathbf{r}'| = \mu - r_0} A(\mathbf{r}') d^2 \mathbf{r}'. \quad (11)$$

If $A(\mathbf{r})$ and $C(\mathbf{r})$ are considered the input and output of a system, respectively, the system is easily shown to be a linear shift-invariant one. So

$$A(\mathbf{r}) * h(\mathbf{r}) = C(\mathbf{r}), \quad (12)$$

where $h(\mathbf{r})$ is the impulse response of the system and $*$ is the continuous convolution. When the input of the system is the 3-D Dirac delta function, the output is $h(\mathbf{r})$. So it can be obtained that

$$h(\mathbf{r}) = \eta \oint_{|\mathbf{r} - \mathbf{r}'| = \mu - r_0} \delta^3(\mathbf{r}') d^2 \mathbf{r}' = \eta \delta(|\mathbf{r}| - \mu + r_0). \quad (13)$$

Accordingly, given that $h(\mathbf{r})$ and $C(\mathbf{r})$ are already known, $A(\mathbf{r})$ can be calculated by a deconvolution approach, which is normally carried out in the frequency domain. Applying 3-D Fourier transform to $A(\mathbf{r})$, $h(\mathbf{r})$, and $C(\mathbf{r})$, we get $\tilde{A}(\boldsymbol{\omega})$, $\tilde{h}(\boldsymbol{\omega})$ and $\tilde{C}(\boldsymbol{\omega})$, respectively. So

$$\tilde{A}(\omega) = \frac{\tilde{C}(\omega)}{\tilde{h}(\omega)}. \quad (14)$$

In fact, $\tilde{h}(\omega)$ is not an elementary function and cannot be given by any algebraic expression. Nevertheless, in the practical application $C(\mathbf{r})$ is constructed from the sampled output of ultrasonic transducer at a series of spatial positions and is therefore in the discrete form. Also, $A(\mathbf{r})$ is discrete, which represents the pixel values of the reconstructed image. So Eq. (14) could be carried out by numerical methods.

Additionally, there may exist some problems if one is directly using Eq. (14) to calculate $\tilde{A}(\omega)$. First, $\tilde{h}(\omega)$ may be zero at some points. Second, the error of $\tilde{C}(\omega)$ will be enlarged at those points where the amplitude of $\tilde{h}(\omega)$ is rather small. As it turns out, an efficient solution is to calculate $\tilde{A}(\omega)$ by [21,22]

$$\tilde{A}(\omega) = \frac{\tilde{C}(\omega)}{\tilde{h}(\omega) \cdot (1 + \lambda/|\tilde{h}(\omega)|^2)}, \quad (15)$$

where λ is a constant.

In sum, the DR algorithm consists of the following steps: to construct $C(\mathbf{r})$ from $p(\mathbf{r}_0, t)$ based on Eqs. (4) and (5); to apply 3-D Fourier transform to $C(\mathbf{r})$, and then $\tilde{C}(\omega)$ is obtained; to calculate $\tilde{A}(\omega)$ based on Eqs. (13) and (15); to apply 3-D inverse Fourier transform to $\tilde{A}(\omega)$, and then $A(\mathbf{r})$ is obtained.

The key step of the DR algorithm is the Fourier-based discrete deconvolution. Using fast Fourier transform (FFT) and inverse fast Fourier transform (IFFT) algorithms, the DR algorithm has fast calculation speed. Moreover, according to Eq. (6), the smaller μ is, the smaller the size of $C(\mathbf{r})$ is. Accordingly, the smaller μ is, the faster the DR algorithm is. However, the error of the DR algorithm will be increased when μ is set to a very small value or the tissue is quite large (with fixed r_0). Therefore, the choice of μ confronts a trade-off between speed and accuracy, which is included in the simulation studies.

B. DR Algorithm for the Limited-View PAT

In the limited-view case, the PAT algorithm is an incomplete data problem of deriving $A(\mathbf{r})$ from $p(\mathbf{r}, t)$ when \mathbf{r} of $p(\mathbf{r}, t)$ does not cover a whole sphere in the 3-D case or a whole circle in the 2-D case.

Without loss of generality, we analyze a simple example in the 1-D case. Assuming

$$[a_0, a_1, a_2] \otimes [h_0, h_1, h_2, h_3] = [c_0, c_1, c_2, c_3, c_4, c_5], \quad (16)$$

where \otimes is the discrete convolution. In the incomplete data deconvolution, we want to derive a_i from all of h_i and part of c_i . It is obviously that a_i can be calculated, if $c_0 \sim c_2$ is known, by solving the following equations:

$$\begin{cases} a_0 \cdot h_0 = c_0 \\ a_0 \cdot h_1 + a_1 \cdot h_0 = c_1 \\ a_0 \cdot h_2 + a_1 \cdot h_1 + a_2 \cdot h_0 = c_2 \end{cases}, \quad (17)$$

when $h_0 \neq 0$.

In the DR algorithm, incomplete $C(\mathbf{r})$ is constructed from the limited-view $p(\mathbf{r}, t)$. Also, Eq. (12) is solvable by listing equations like Eq. (17), the only difference being that the image reconstruction is a 3-D or a 2-D case. As shown by the following simulation studies, in the 2-D case detected signals over 90° are enough to reconstruct an approximate image by the DR algorithm.

However, in the DR algorithm the discrete deconvolution had better not be solved in the time domain like Eq. (17). On the one hand, in practical applications the resolution of $C(\mathbf{r})$ and $A(\mathbf{r})$ is always quite large, which will create difficulty in solving the equations. On the other hand, it is well known that the time-domain deconvolution is very sensitive to data noise. Therefore, an efficient approach is to carry out the deconvolution in the frequency domain, described as follows.

Assume that the resolution of $A(\mathbf{r})$ is $M_1 \times M_2 \times M_3$ and the resolution of the incomplete $C(\mathbf{r})$ is $N_1 \times N_2 \times N_3$, satisfying that $N_1 > M_1$, $N_2 > M_2$, $N_3 > M_3$. Obviously only $N_1 \times N_2 \times N_3$ points of $h(\mathbf{r})$ are used in the incomplete convolution, which is defined as $h'(\mathbf{r})$. The convolution of $A(\mathbf{r})$ and $h'(\mathbf{r})$ has the size $(N_1 + M_1 - 1) \times (N_2 + M_2 - 1) \times (N_3 + M_3 - 1)$, and its partial region with the first $N_1 \times N_2 \times N_3$ values is exactly $C(\mathbf{r})$. Then the incomplete $C(\mathbf{r})$ is filled with zeros (sometimes gradually smoothing the data to zero at the boundary in order to reduce artifacts in the reconstruction) to the size $(N_1 + M_1 - 1) \times (N_2 + M_2 - 1) \times (N_3 + M_3 - 1)$, defined as $C'(\mathbf{r})$. So

$$A(\mathbf{r}) \otimes h'(\mathbf{r}) \approx C'(\mathbf{r}). \quad (18)$$

Then $A(\mathbf{r})$ can be calculated by FFT and IFFT algorithms as in Eq. (15). The accuracy and robustness to noise of this approach will be validated in the simulation studies.

C. Two Popular PAT Algorithms

In the following simulation studies, the DR algorithm is compared with two popular PAT algorithms, the time-domain reconstruction (TDR) [12,15] and the filtered back projection (FBP) [11,17]. The TDR is an exact algorithm proposed in 2002; and the FBP, proposed as early as in 1995, is an approximate algorithm based on the Radon transform and is shown to work well for the limited-view PAT [20].

These two algorithms were both originally proposed for the full-view PAT. In the limited-view PAT, $p(\mathbf{r}, t)$ is concatenated with zeros in both algorithms. If one point of the scanned object is detected over the solid angle Ω in the 3-D case (angle θ in the 2-D case), a useful correction is to compensate that point's value by multiplying the reconstructed function by a factor $4\pi/\Omega$ ($2\pi/\theta$ in the 2-D case) [20].

3. RESULTS AND DISCUSSION

A. Simulation Method

The computer simulation is conducted with Matlab programs. First, the model of the scanned tissue is estab-

lished. Second, excited photoacoustic signals are simulated by the finite-difference time-domain method [23]. Finally, the tissue image is reconstructed from the simulated signals (with and without noise).

The simulation is conducted in the 2-D case to reduce computational complexity. The extension of conclusions of the 2-D case to a 3-D one is straightforward. However, in the 3-D case the attenuation of the acoustic signal originating from a point is proportional to $1/r$, while in the 2-D case the attenuation is proportional to $1/\sqrt{r}$ [16]. Accordingly, in the 2-D DR algorithm, Eq. (4) should be rewritten as

$$S(\mathbf{r}_0, t) = \left[\int_0^t p(\mathbf{r}_0, t) dt \right] \cdot \sqrt{t}, \quad (19)$$

while other steps are the same.

B. Full-View PAT

The given electromagnetic absorption of the simulated tissue is shown in Fig. 1(a). The image size is 15 mm \times 15 mm. The ultrasonic transducer with a sampling rate of 20 MHz detects signals along a circle whose radius is 7.5 mm, with the angle step of 2.25°.

The reconstructed images using the TDR, FBP, and DR algorithms are shown in Figs. 1(b)–1(j), with different levels of zero-mean Gaussian noise added to simulated photoacoustic signals. As shown by Fig. 1, the accuracy of the DR algorithm is as good as that of the TDR and the FBP, no matter what level of noise is added. That is, the DR algorithm is precise and not sensitive to data noise. The

difference among three algorithms' accuracy and robustness to noise is so small that it could hardly be assessed by the naked eye.

In the DR algorithm, the parameter μ in Eq. (5) is set to the minimum value: $2r_0$. Although the error of the DR algorithm will be increased theoretically when μ is set to a small value or the tissue is large (compared with the scanning radius), the results in Fig. 1 demonstrate that the DR algorithm has good precision, nearly equivalent to that of the TDR and the FBP, for a large tissue with the minimum μ . Moreover, the minimum μ brings the fastest speed. Therefore, the optimum value of μ is $2r_0$ in the full-view PAT.

A further study is conducted to quantitatively compare the precision of the three algorithms for tissues of various sizes. Square tissues are simulated, and their reconstructed images are evaluated by the peak signal-to-noise ratio (PSNR). Results are shown in Fig. 2, where r_0 is the scanning radius and r' is the farthest distance between the tissue and the center of scanning circle. Different levels of noise are added to simulated photoacoustic signals. It can be seen in Fig. 2 that when no noise is added, the PSNR of the DR is a bit lower than that of the TDR and a bit higher than that of the FBP if r'/r_0 is smaller than 76%. If the tissue is so large that r'/r_0 exceeds 76%, the PSNR of the DR is the lowest, which is in accordance with the theoretical prediction. When 6% noise is added, the PSNR of the TDR declines more than those of the FBP and DR. As a result, the PSNR of the DR is the highest when r'/r_0 is smaller than 60%. This is because the calculations in the TDR are based on the differential of p , in

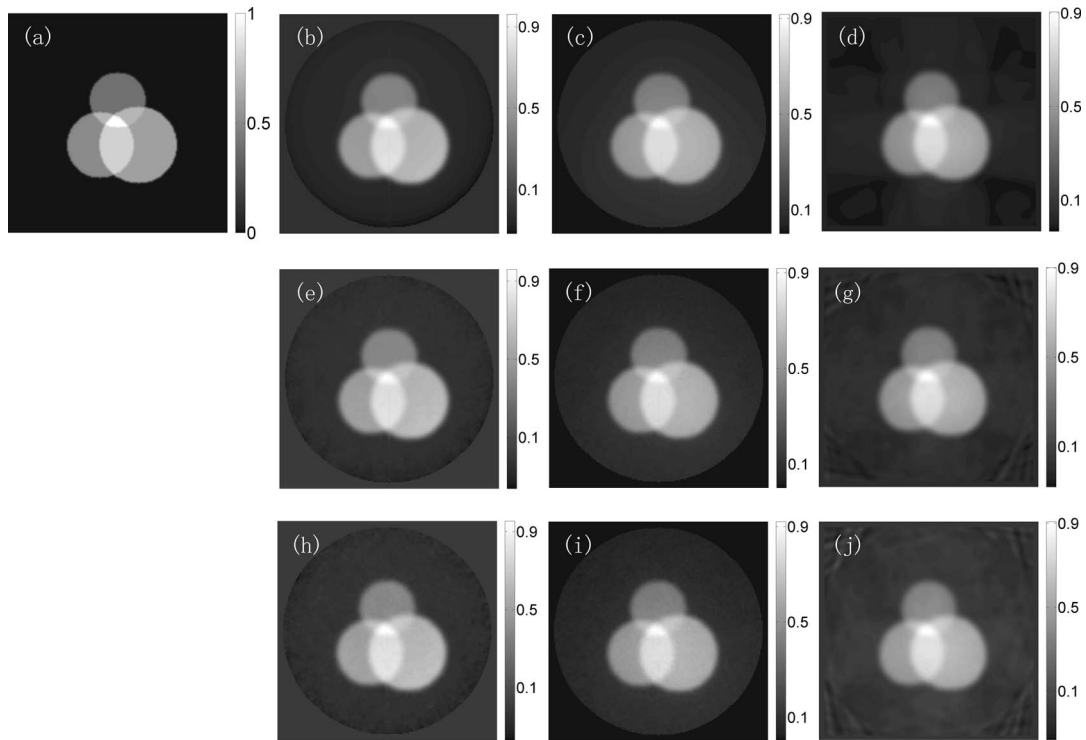


Fig. 1. (a) Original image and (b)–(j) reconstructed images of the simulated tissue with different levels of Gaussian noise added (the grayscale denotes the value of the electromagnetic absorption). The three rows from top to bottom, except (a), correspond to reconstructed images with no noise, 6% noise, and 12% noise, respectively. (b), (e), and (h) TDR results, (c), (f), and (i) FBP results, (d), (g), and (j) DR results.

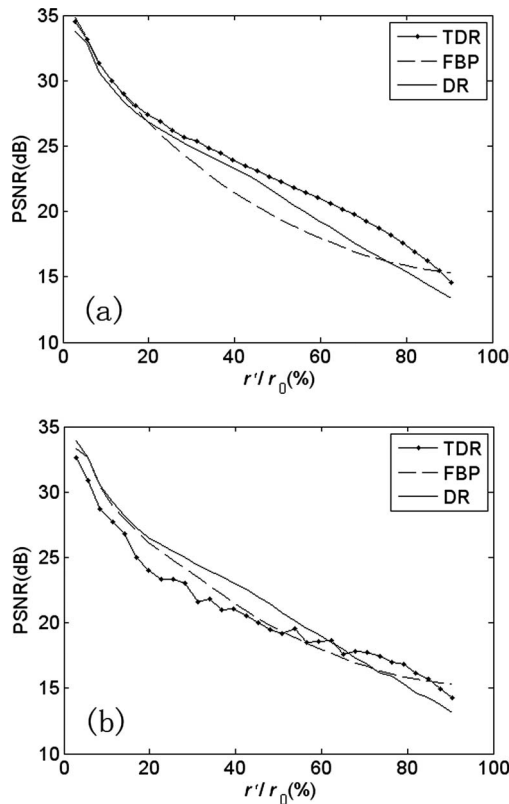


Fig. 2. PSNR of reconstructed images of square tissues by three algorithms with various r'/r_0 , with (a) no noise added and (b) 6% noise added.

which the noise is increased, yet the FBP and DR are both based on the integral of p , in which the noise is counteracted.

The calculation time costs by the TDR, FBP, and DR algorithms are compared in a computer (Intel Pentium 4 processor with a clock frequency of 2.0 GHz) with Matlab programs. Results of various reconstruction resolutions are shown in Table 1. It can be found that the DR algorithm is more than ten times faster than the TDR and the FBP, the chief reason being that the key step of the DR algorithm is the discrete deconvolution which can be calculated very quickly by FFT and IFFT algorithms.

C. Limited-View PAT

In the DR algorithm of the limited-view PAT, the resolution of $C(\mathbf{r})$ is proportional to the scanning angle and the parameter u as shown in Eq. (5). While the resolution of $C(\mathbf{r})$ decreases with the loss of $p(\mathbf{r}, t)$, u should be set to a larger value than in the full-view case ($\mu=2r_0$) in order to strike a balance, since the extremely low resolution of $C(\mathbf{r})$ would result in large errors. It is shown by simulation studies that $\mu=3r_0$ is a good choice.

The given electromagnetic absorption distribution of the simulated tissue is shown in Fig. 3. The image size is 15 mm \times 15 mm. The ultrasonic transducer detects signals along a circle whose radius is 7.5 mm, with the angle step of 2.25°. We define the angle with the coordinate (x, y) as follows: (7.5, 0) is 0°, (0, -7.5) is 90°, (-7.5, 0) is 180°, and (0, 7.5) is 270°.

The reconstructed images of the TDR, FBP, and DR algorithms with different scanning angles are shown in Fig.

Table 1. Time Cost by Three Algorithms with Various Reconstruction Resolutions

Reconstruction Resolution	Time Cost (s)		
	TDR	FBP	DR
50 \times 50	0.36	0.41	0.025
100 \times 100	1.2	1.3	0.091
200 \times 200	4.7	5.4	0.38
300 \times 300	11	12	0.89
400 \times 400	19	21	1.7

4 (with the same coordinates as Fig. 3). The two rows from top to bottom correspond to the scanning angles of 90° (from 0° to 90°) and 135° (from 0° to 135°). The three columns from left to right correspond to the results of the TDR, FBP, and DR algorithm, respectively. As shown in Fig. 4, the reconstructed images of the DR algorithm are superior to those of the TDR and FBP, with clearer boundaries and fewer artifacts. The effect of boundary blurring is explained in [20]. Moreover, the smaller the scanning angle, the more obvious the superiority of the DR algorithm. This is because the detected signals over 90° are enough to reconstruct an approximate image in the DR algorithm, but the TDR and FBP both need full-view signals. However, the DR algorithm is an approximate one, and the error will increase with the decrease of scanning angles, as shown in Fig. 4.

The profiles through the original image (Fig. 3) and reconstructed images (Fig. 4) along two transects ($x=2.3$ mm and $y=0$ mm) are shown in Fig. 5. Obviously the DR algorithm is quantitatively more accurate than the TDR and FBP for the limited-view PAT. Generally all these algorithms show the accurate contrast level, but the TDR and FBP results have more fluctuations and larger errors at the same level and change more slowly between different levels compared with the DR results.

The robustness of the DR algorithm for the limited-view PAT is also verified by adding zero-mean Gaussian noise to simulated photoacoustic signals. Figure 6 shows the reconstructed images of the TDR, FBP, and DR algorithms with 6% noise added. Comparing Fig. 6 with Fig. 4, it can be found that the DR algorithm presents stronger robustness to noise than the TDR and FBP in the limited-view PAT.

The DR algorithm treats PAT as a discrete problem and aims at calculating limited pixel values of the reconstructed image. The plain fact is that most other algo-

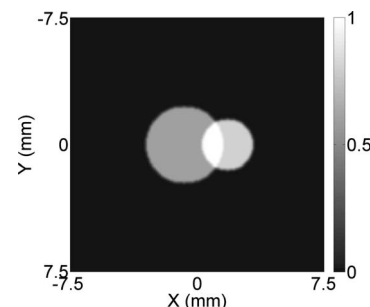


Fig. 3. The given electromagnetic absorption distribution (shown by grayscale) of the simulated tissue.

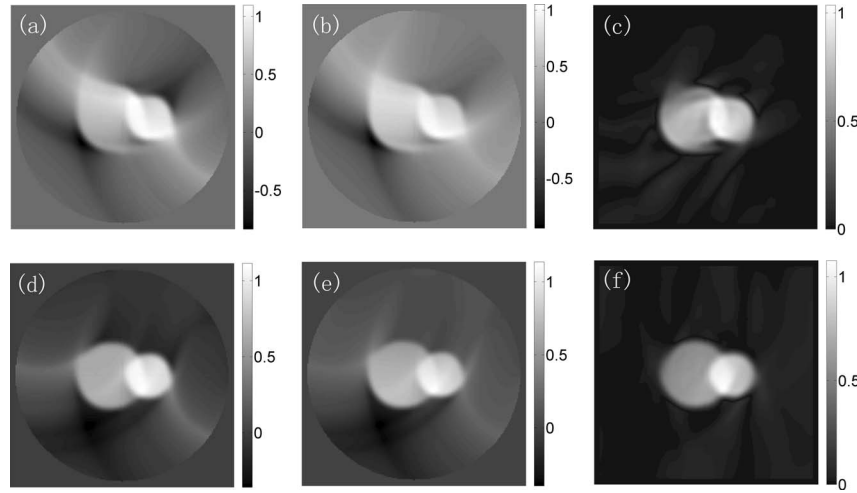


Fig. 4. Reconstructed images of the tissue (as shown in Fig. 3). The two rows from top to bottom correspond to the scanning angles of 90° (from 0° to 90°) and 135° (from 0° to 135°); the three columns from left to right correspond to the results of the TDR, FBP, and DR.

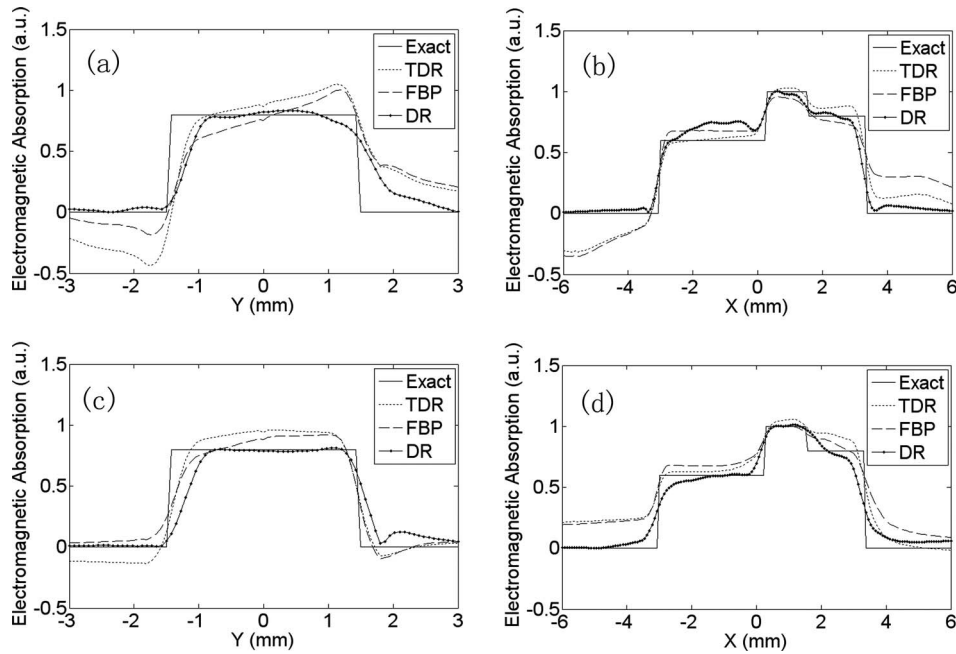


Fig. 5. Profiles through the original image (as shown in Fig. 3) and reconstructed images (as shown in Fig. 4) along two transects. (a) 90° scanning, along $x=2.3$ mm, (b) 90° scanning, along $y=0$ mm, (c) 135° scanning, along $x=2.3$ mm, (d) 135° scanning, along $y=0$ mm.

gorithms, such as the TDR and the FBP, treat PAT as an analytical problem and aim at obtaining the analytical relation between the tissue's electromagnetic absorption distribution and detected photoacoustic signals, which is much more difficult than the discrete problem. It has been shown that although an arbitrarily small scanning arc suffices for the uniqueness of recovery [20,24], the process of computing unmeasured signals from limited-view signals is unstable [25,26]. So the exact analytical method is not suitable for the limited-view PAT. Yet the DR algorithm starts from sampled photoacoustic signals whose high-frequency components are eliminated. Accordingly, only relatively low-frequency components in the image are reconstructed on the basis of numerical approaches. In fact, reconstruction of the high-frequency components

has proved to be the cause of instability in the limited-view PAT [25]. In other words, the DR algorithm avoids the difficult problem of exactly reconstructing high-frequency components and seeks a near-optimal solution. These may be the reasons why the DR algorithm is an efficient one for the limited-view PAT.

4. CONCLUSION

The DR algorithm is proposed as an approximate algorithm for the full-view and limited-view PAT. It is demonstrated theoretically that the DR algorithm is computationally efficient and is suitable for the limited-view PAT, yet the error of the DR algorithm increases with the size of the detected object. Simulation results prove our theory

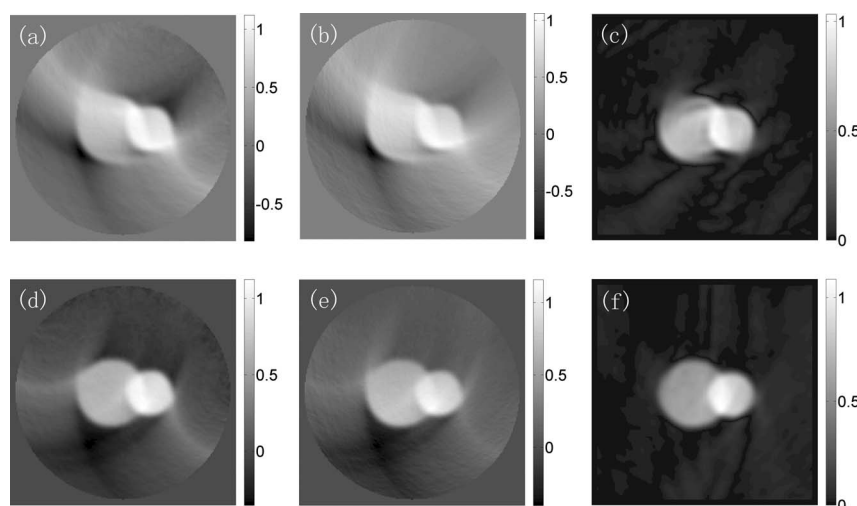


Fig. 6. Reconstructed images of the tissue (as shown in Fig. 3) with 6% noise added. The two rows from top to bottom correspond to the scanning angles of 90° (from 0° to 90°) and 135° (from 0° to 135°), and the three columns from left to right correspond to the results of the TDR, FBP, and DR.

and show that in the full-view PAT the DR algorithm has good precision and strong robustness to noise, nearly equivalent to those of the TDR and the FBP even for relatively large objects. Yet the DR is more than ten times faster than the TDR and FBP due to the available FFT and IFFT algorithms. In the limited-view case, it is shown that reconstructed images of the DR algorithm are superior to those of the TDR and FBP with clearer boundaries, fewer artifacts, and stronger robustness to noise. Here the smaller the scanning angle, the more obvious the superiority of the DR algorithm.

ACKNOWLEDGMENTS

This work was supported by the National Basic Research Program of China (No. 2006CB705707), Natural Science Foundation of China (NSFC) (No. 30570488) and Shanghai Leading Academic Discipline Project (No. B112).

REFERENCES

1. H. F. Zhang, K. Maslov, G. Stoica, and L. V. Wang, "Functional photoacoustic microscopy for high-resolution and noninvasive in vivo imaging," *Nat. Biotechnol.* **24**, 848–851 (2006).
2. K. H. Song, G. Stoica, and L. V. Wang, "In vivo three-dimensional photoacoustic tomography of a whole mouse head," *Opt. Lett.* **31**, 2453–2455 (2006).
3. J. J. Niederhauser, M. Jaeger, R. Lemor, P. Weber, and M. Frenz, "Combined ultrasound and optoacoustic system for real-time high-contrast vascular imaging in vivo," *IEEE Trans. Med. Imaging* **24**, 436–440 (2005).
4. K. Maslov, G. Stoica, and L. V. Wang, "In vivo dark-field reflection-mode photoacoustic microscopy," *Opt. Lett.* **30**, 625–627 (2005).
5. C.-W. Wei, S.-W. Huang, C.-R. C. Wang, and P.-C. Li, "Photoacoustic flow measurements based on wash-in analysis of gold nanorods," *IEEE Trans. Ultrason. Ferroelectr. Freq. Control* **54**, 1131–1141 (2007).
6. M. Xu and L. V. Wang, "Photoacoustic imaging in biomedicine," *Rev. Sci. Instrum.* **77**, 041101-1-22 (2006).
7. A. A. Karabutov, V. G. Andreev, B. Bell, R. D. Fleming, Z. Gatalica, M. Motamedi, E. V. Savateeva, H. Singh, S. V. Solomatin, S. L. Thomsen, P. M. Henrichs, and A. A. Oraevsky, "Optoacoustic images of early cancer in forward and backward modes," *Proc. SPIE* **4434**, 13–27 (2001).
8. R. G. M. Kolkman, E. Hondebrink, W. Steenbergen, and F. F. M. Mul, "In vivo photoacoustic imaging of blood vessels using an extreme-narrow aperture sensor," *IEEE J. Sel. Top. Quantum Electron.* **9**, 343–346 (2003).
9. R. Zemp, R. Bitton, M.-L. Li, K. K. Shung, and L. V. Wang, "Imaging microvascular dynamics noninvasively with realtime photoacoustic microscopy," *Proc. SPIE* **6430**, 643015 1–8 (2007).
10. X. Wang, Y. Pang, G. Ku, X. Xie, G. Stoica, and L. V. Wang, "Noninvasive laser-induced photoacoustic tomography for structural and functional in vivo imaging of the brain," *Nat. Biotechnol.* **7**, 803–806 (2003).
11. R. A. Kruger, P. Liu, Y. Fang, and C. R. Appledom, "Photoacoustic ultrasound (PAUS)-reconstruction tomography," *Med. Phys.* **22**, 1605–1609 (1995).
12. M. Xu and L. V. Wang, "Time-domain reconstruction for thermoacoustic tomography in a spherical geometry," *IEEE Trans. Med. Imaging* **21**, 814–822 (2002).
13. Y. Xu, D. Feng, and L. V. Wang, "Exact frequency-domain reconstruction for thermoacoustic tomography-I: planar geometry," *IEEE Trans. Med. Imaging* **21**, 823–828 (2002).
14. Y. Xu, M. Xu, and L. V. Wang, "Exact frequency-domain reconstruction for thermoacoustic tomography-II: cylindrical geometry," *IEEE Trans. Med. Imaging* **21**, 829–833 (2002).
15. M. Xu and L. V. Wang, "Universal back-projection algorithm for photoacoustic computed tomography," *Phys. Rev. E* **71**, 016706-1–7 (2005).
16. K. P. Kostli and P. C. Beard, "Two-dimensional photoacoustic imaging by use of Fourier-transform image reconstruction and a detector with an anisotropic response," *Appl. Opt.* **42**, 1899–1908 (2003).
17. M. Haltmeier, T. Schuster, and O. Scherzer, "Filtered backprojection for thermoacoustic computed tomography in spherical geometry," *Math. Methods Appl. Sci.* **28**, 1919–1937 (2005).
18. H. Jiang, Z. Yuan, and X. Gu, "Spatially varying optical and acoustic property reconstruction using finite-element-based photoacoustic tomography," *J. Opt. Soc. Am. A* **23**, 878–888 (2006).
19. L. A. Kunyansky, "Explicit inversion formulae for the spherical mean Radon transform," *Inverse Probl.* **23**, 373–383 (2007).
20. Y. Xu and L. V. Wang, "Reconstructions in limited-view thermoacoustic tomography," *Med. Phys.* **31**, 724–733 (2004).
21. S. M. Riad, "The deconvolution problem: an overview," *Proc. IEEE* **74**, 82–85 (1986).

22. A. Bennis and S. M. Riad, "An optimization technique for iterative frequency-domain deconvolution," *IEEE Trans. Instrum. Meas.* **39**, 358–362 (1990).
23. D.-H. Huang, C.-K. Liao, C.-W. Wei, and P.-C. Li, "Simulations of optoacoustic wave propagation in light-absorbing media using a finite-difference time-domain method," *J. Acoust. Soc. Am.* **117**, 2795–2801 (2005).
24. M. L. Agranovsky and E. T. Quinto, "Injectivity sets for the radon transform over circles and complete systems of radial functions," *J. Funct. Anal.* **139**, 383–414 (1996).
25. S. K. Patch, "Thermoacoustic tomography—consistency conditions and the partial scan problem," *Phys. Med. Biol.* **49**, 2305–2315 (2004).
26. V. P. Palamodov, "Reconstruction from limited data of arc means," *J. Fourier Anal. Appl.* **6**, 25–42 (2000).